



Analysis of microstructure and texture evolution in pure magnesium during symmetric and asymmetric rolling

Benoît Beausir^{a,*}, Somjeet Biswas^a, Dong Ik Kim^b, László S. Tóth^c, Satyam Suwas^a

^a Department of Materials Engineering, Indian Institute of Science, Bangalore 560 012, India

^b Korea Institute of Science and Technology, 136791 Seoul, Republic of Korea

^c Laboratoire de Physique et Mécanique des Matériaux, Université de Metz, Ile du Saulcy, 57045 Metz, France

Received 13 May 2009; received in revised form 3 July 2009; accepted 5 July 2009

Available online 7 August 2009

Abstract

Asymmetric rolling of commercially pure magnesium was carried out at three different temperatures: room temperature, 200 °C and 350 °C. Systematic analysis of microstructures, grain size distributions, texture and misorientation distributions were performed using electron backscattered diffraction in a field emission gun scanning electron microscope. The results were compared with conventional (symmetric) rolling carried out under the same conditions of temperature and strain rate. Simulations of deformation texture evolution were performed using the viscoplastic self-consistent polycrystal plasticity model. The main trends of texture evolution are faithfully reproduced by the simulations for the tests at room temperature. The deviations that appear for the textures obtained at high temperature can be explained by the occurrence of dynamic recrystallization. Finally, the mechanisms of texture evolution in magnesium during asymmetric and symmetric rolling are explained with the help of ideal orientations, grain velocity fields and divergence maps displayed in orientation space.

© 2009 Acta Materialia Inc. Published by Elsevier Ltd. All rights reserved.

Keywords: Asymmetric rolling; Symmetric rolling; HCP; Textures; Magnesium

1. Introduction

Magnesium and its alloys have high potential in automobile and aerospace applications due to their superior specific strength and density [1,2] compared with other metals.

However, the processing of magnesium and its alloys is relatively difficult at ambient temperature due to their limited ductility, which is essentially attributed to the limited number of slip systems owing to the hexagonal crystal structure. Severe plastic deformation processes (SPD) can improve formability [3] and the following major SPD techniques are currently used in laboratory studies: equal channel angular extrusion (ECAE) [4–8], high pressure torsion

(HPT) [9–11] and accumulative roll bonding (ARB) [12–14]. It is now well known that the formation of basal texture away from the rolling plane as well as a decrease in grain size can increase the formability of magnesium [15]. SPD processes like ECAE have been known to produce texture with a strong basal component located at 45° between ED and ND. However, in the conventional sense, it is only applicable for rod products. The application base, however, is more extended for flat products, which essentially require the rolling behaviour to be improved. One such process can be asymmetric rolling (ASR) or accumulative roll bonding (ARB), which amalgamates the ideas derived from SPD processes with rotating the basal plane away from the rolling plane. Both ARB and ASR are associated with a shear deformation in addition to the deformation in plane strain compression during symmetric rolling (SR). However, in these two pro-

* Corresponding author.

E-mail address: benoit.beausir@univ-metz.fr (B. Beausir).

cesses the additional shear component is not achieved in a sheet in the same way. In ASR the shear strain results from a difference in velocity between the bottom and top surfaces of the sheet, leading to shear strain in the whole thickness of the sheet in one pass. In ARB the shear strain is produced by friction between the rollers and the sheet and affects only the surface layer in one pass. Then, during subsequent passes, due to the bonding process, the surface shear texture extends into the bulk, leading, after several passes, to a global shear texture component in the sheet.

Several investigations into the microstructure of and texture evolution in magnesium alloys can be found in the literature [16–22]. However, the mechanism of texture evolution, occurrence of dynamic recrystallization or ideal position, and their persistence characteristics are not yet well understood. The analysis of these characteristics is helpful in understanding the texture evolution differences between ASR and SR and could help proposing appropriate asymmetric rolling strategies in order to change the final texture and thus modify the mechanical properties of rolled sheets.

In the present investigation asymmetric rolling of commercially pure magnesium was carried at different temperatures and the evolution of texture has been studied and compared with conventional (symmetric) rolling under at same temperature and strain rate. In the ASR process the circumferential velocities of the upper and lower rollers are different, so shear deformation is applied throughout the thickness of the sheet [23–27]. Different circumferential velocities can be achieved by three ways: (i) rollers with different radii; (ii) rollers with different angular velocities; and (iii) different lubrication conditions between the sheet and each of the two rollers. In our case rollers with different radii were used to apply the additional shear deformation throughout the thickness of the sheet.

Section 2 of this paper presents the experimental details. A thorough analysis of the microstructure, grain size distributions, misorientation distributions and texture evolution after ASR and SR is presented in Section 3. Section 4 presents the simulation conditions and a comparison with experimental texture evolution is performed. In Section 5 the mechanism of texture evolution is discussed in terms of ideal orientations, grain velocity field and divergence maps in orientation space. Finally, in Section 6 the effect of dynamic recrystallization on texture is discussed in terms of plastic energy.

2. Experimental details

Cast magnesium billets of 99.93% purity were hot forged at 450 °C to obtain plates with a thickness of 40 mm. The

Table 1
Material composition (wt.%).

Mg	Al	Mn	Cu	Fe	Si	Ni
99.93	0.0032	0.0128	0.0005	0.0017	0.0228	0.0003

nominal composition of the as received material is shown in Table 1. The microstructure of the material after forging was composed of grains with an average size of $\sim 14 \mu\text{m}$ with very weak texture. Rolling billets of $20 \times 75 \text{ mm}$ cross-section and 10 mm thickness were extracted from the forged plates. The samples were machined in such a manner that one end had a wedge shape with an angle of 30° (see Fig. 1). This was done in order to impart a high level of rolling reduction in one pass. In order to quantify the additional shear components induced in the sheet by ASR, vertical inserts of magnesium were placed in the samples (Figs. 1 and 2).

Rolling, both asymmetric and symmetric, was carried out at 350 °C, 200 °C and room temperature (RT). In both cases (SR and ASR) two passes with $\sim 50\%$ reduction in thickness were performed and a final thickness of 2.5 mm was obtained. In the case of ASR the upper and the lower rollers had different diameters (165 and 110 mm). Both rollers rotated at 53 rpm, so that the circumferential velocity of the bigger roll was 0.92 m s^{-1} and for the smaller roll was 0.61 m s^{-1} . This led to an average velocity of $\sim 0.76 \text{ m s}^{-1}$, which is almost same as the velocity imparted during SR. While carrying out symmetric (or conventional) rolling the same velocity was imparted to two rollers of the same size. The roller speed was 63 rpm, giving a circumferential velocity of 0.73 m s^{-1} . In both ASR and SR the samples were heat treated at the respective rolling temperatures before rolling. The temperature was measured at the centre of the specimen with the help of a thermocouple positioned inside a 1.5 mm hole (Fig. 1). The processing schedules for both ASR and SR are summarized in Table 2.

The microstructure and texture of the as received as well as the ASR and SR samples were examined by electron backscattered diffraction (EBSD) technique using a FEI-Sirion field emission gun (FEG) scanning electron microscope (SEM). All the samples were sectioned along the TD plane and the EBSD scans were performed at the centre of the sheet. The specimens were prepared by polishing on emery paper up to 6 μm roughness. This was followed by chemical polishing with 75% ethane diol, 24% distilled water and 1% HNO_3 on a cloth. After achieving the desired surface finish the specimens were electro-polished in a 3:5 volume fraction of ortho-phosphoric acid and ethanol in an electro-polishing unit with a stainless steel cathode at 3 V for 30 s and 1.5 V for 2 min. EBSD was carried out at a step size of 0.5 μm . The microstructural characteristics,

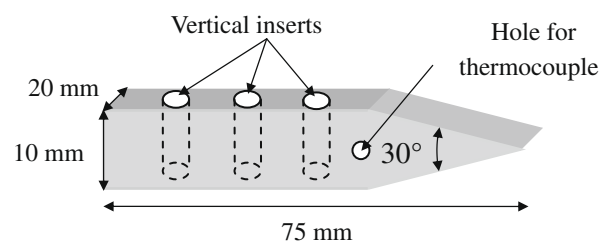


Fig. 1. Initial shape of the samples.

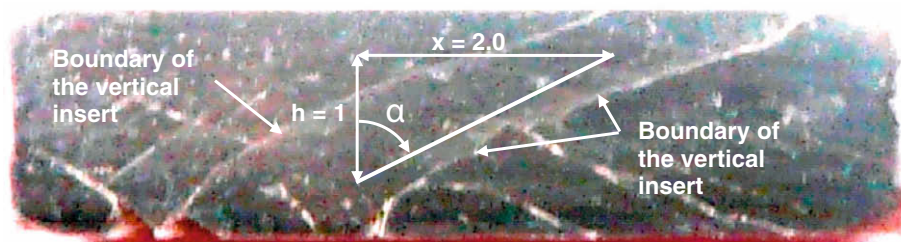


Fig. 2. Shape of the vertical insert after the first pass of asymmetric rolling.

including texture evolution, grain size distribution and misorientation angle distributions, were calculated for each sample.

3. Experimental results

3.1. Microstructure

Fig. 3 shows the microstructure maps obtained by EBSD in the TD plane on the half-thickness areas of sheets. The colour code corresponds to the orientation of the TD axis with respect to the crystal reference system. Grain boundaries were identified with a minimum of 15° misorientation across the boundary. The microstructures of both the ASR and SR samples rolled to 75% at 200 °C and 350 °C showed equiaxed grains with serrated (or zig-zag) grain boundaries. The serrated boundaries were clearly seen in the EBSD generated microstructures recorded at higher magnification. However, the room temperature ASR and SR samples showed a mixture of small equiaxed grains with high angle grain boundaries and larger elongated grains. The average grain sizes for each of the samples are presented in Table 3. The average grain size increased with rolling temperature for both the ASR and SR samples. However, the grain sizes of the ASR and SR samples were almost the same at a given temperature.

Fig. 4 presents the grain size distributions for the materials prior to rolling and after rolling (for both ASR and SR). For all the samples the grain size distributions displayed a singular peak. However, it is worth noting that in all the ASR samples the range of grain size was wider compared with the SR samples for any temperature. A slight increase in the average grain size of the ASR samples can be attributed to the increase in the span of the grain size spectrum (see Table 3). It should be noted that the grain size data presented in Table 3 was obtained by the

number fraction method [28] (a method analogous to the random point counting method conventionally used for grain size estimation). In contrast, the distribution shown in Fig. 4 was derived using the area fraction method [28], which was used in order to explore the nature of the distribution (for example, unimodal or bimodal). However, in the case of the room temperature ASR and SR samples a difference in the range of grain sizes was much less and was barely discernible. In this case the average grain size of the ASR sample was less than that of its counterpart SR sample.

In order to examine the occurrence of any restoration process, misorientation between each pair of neighbouring grains was calculated. Fig. 5 shows the misorientation distribution of the first neighbours (also called the Mackenzie correlated misorientation distribution) for the ASR and SR samples after the second pass. Values below the critical 15° misorientation angle appear, because the average orientation of the grain is used, which is different from the misorientation at the grain boundary due to lattice curvature within the grain. It was observed that a large number of the grains were misoriented by $\sim 30^\circ$ for all the deformed samples. In order to determine the misorientation axes, their projection for grains misoriented in the range 27.5° – 32.5° are also plotted in Fig. 5. For brevity, the projections for only two samples are shown: ASR room temperature and SR at 200 °C samples. However, the other samples showed similar results. From these figures it is clear that the misorientation axes are mostly close to the c -axis of the hexagonal lattice.

3.2. Texture

Fig. 6a and b presents the (10.0), (11.0) and (00.2) pole figures of the ASR and SR samples obtained from the EBSD data after the second pass, along with the simulation

Table 2
Experimental sequences.

	Heat treatment	1st pass (10 → 5 mm)	Heat treatment	2nd pass (5 → 2.5 mm)
350 °C	370 °C for 10 min, cooled to 350 °C in 15 s	Temperature reduced to 330 °C	360 °C for 3 min	Temperature reduced to 330 °C
200 °C	220 °C for 10 min, cooled to 200 °C in 15 s	Temperature reduced to 180 °C	210 °C for 3 min	Temperature reduced to 180 °C
Room temperature	None	Room temperature	None	Room temperature

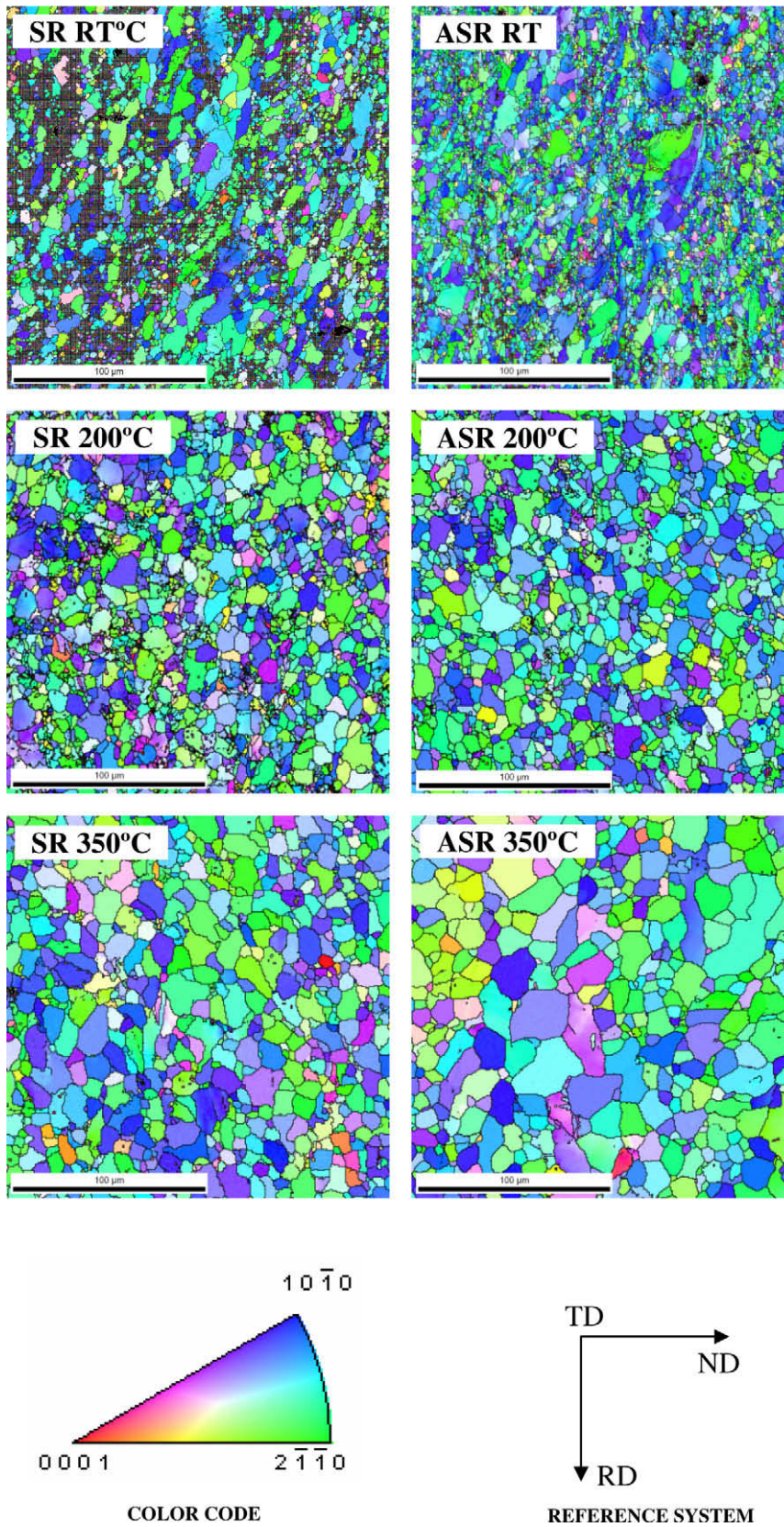


Fig. 3. Microstructures obtained by EBSD after two passes of rolling.

results (presented in the next section). In all these pole figures rolling direction (RD) is towards the right, the normal direction (ND) is on the top and the transverse direc-

tion (TD) is the projection plane. In the case of the SR samples a predominant basal texture $[00.2]||ND$ developed at all temperatures. However, in the case of the ASR sam-

Table 3
Average grain sizes (μm).

Starting material	14.1		
SR Room temperature	2.25	ASR Room temperature	2.11
SR 200 °C	3.39	ASR 200 °C	3.95
SR 350 °C	5.57	ASR 350 °C	6.74

ples the basal fibre is rotated by ~5–10° anticlockwise from the ND. For a better representation, the experimental textures have also been plotted in Euler orientation space (see Figs. 7a–c and 8a–c). It can be seen in the $\varphi = 90^\circ$ sections that the distribution of the grains in the φ_2 direction depends on the test temperature for both ASR and SR. Concerning the reference system for the Euler angles, a Cartesian system was fixed to the unit cell of the hexagonal crystal structure so that the testing direction axes X (RD), Y (TD) and Z (ND) were parallel to the crystallographic axes of the [10.0], [11.0] and [00.2] directions, respectively, of a non-rotated crystal (this convention will be used in all the figures in this work).

4. Deformation texture simulations

Several descriptions of deformation by streamlines after asymmetric or conventional rolling have been proposed in the literature [29–32]. From such streamlines a variable velocity gradient in the die can be extracted that describes in detail the deformation of a material element during the process. This type of modelling is appropriate to simulate texture heterogeneities through the thickness of a sheet. The curvature of the streamline accounts for a shear component with the shear plane being the RD plane and the shear direction parallel to ND. In the middle of the sheet the impact of curvature of the flow line in this shear is negligible. Another shear component, nearly constant within the sheet, is also generated by the different circumferential velocities of the rollers and operates in the ND plane and in the RD direction [33–37]. This approach is also adopted in the present work.

In conventional rolling the state is nearly plane strain and the following constant velocity gradient is used (compression in ND; $\dot{\epsilon} < 0$ and tension in RD):

$$L = \begin{pmatrix} -\dot{\epsilon} & 0 & 0 \\ 0 & 0 & 0 \\ 0 & 0 & \dot{\epsilon} \end{pmatrix}_{x,y,z} \quad (1)$$

In ASR, a shear component is imposed on the sheet by the different speeds of the rollers and the velocity gradient becomes:

$$L = \begin{pmatrix} -\dot{\epsilon} & 0 & -p\dot{\epsilon} \\ 0 & 0 & 0 \\ 0 & 0 & \dot{\epsilon} \end{pmatrix}_{RD,TD,ND} \quad (2)$$

Here the shear rate is $\dot{\gamma} = -p\dot{\epsilon}$, with $p > 0$ being the shear coefficient that characterizes the contribution of shear with respect to rolling strain. In the following it is assumed that

the velocity gradient is stationary during a rolling pass, meaning that p is constant. In order to evaluate p we use our experimental observations; see Fig. 2, where an initially vertical insert becomes inclined progressively by an angle α with respect to the ND direction due to the combined effect of shear and compression. The shear angle is defined by:

$$\tan(\alpha) = \frac{x}{h} \quad (3)$$

The time derivative of Eq. (3) is:

$$\frac{\dot{\alpha}}{\cos^2 \alpha} = \frac{\dot{x}}{h} - \frac{\dot{h}}{h} \frac{x}{h} \quad (4)$$

Using the relations $\dot{x}/h = \dot{\gamma}$, $\dot{\gamma} = -p\dot{\epsilon}$ and $\dot{\epsilon} = \dot{h}/h$ as well as Eq. (3) we obtain the following integral:

$$\int_0^{\alpha_f} -\frac{d\alpha}{(p + \tan \alpha) \cos^2 \alpha} = \int_{h_i}^{h_f} \frac{dh}{h} \quad (5)$$

Here h_i and h_f are the initial and final thickness of the sheet, respectively, and α_f is the final inclination angle of the insert (see Fig. 2). The shear coefficient can be obtained by solving Eq. (5):

$$p = \frac{h_f}{h_i - h_f} \tan(\alpha_f) \quad (6)$$

In the present case $h_i = 5$ mm, $h_f = 2.5$ mm and $\tan(\alpha_f) \cong 2$, which leads to a value of $p \cong 2$. Note that for the particular case of a reduction of 50% $p = \tan(\alpha_f)$.

The obtained velocity gradient is inserted into the viscoplastic polycrystal self-consistent model to simulate the texture evolution. As the initial texture was very weak, 2000 randomly distributed spherical grains were used for the simulations. Several slip system families are present in the hexagonal structured materials. They are: basal $\{0001\} \langle 1210 \rangle$, prismatic $\{1\bar{1}00\} \langle 1120 \rangle$, pyramidal (a) $\{10\bar{1}1\} \langle \bar{1}2\bar{1}0 \rangle$, pyramidal $\langle c+a \rangle$ type I $\{10\bar{1}1\} \langle 2\bar{1}\bar{1}3 \rangle$ and pyramidal $\langle c+a \rangle$ type II $\{2\bar{1}\bar{1}2\} \langle 2\bar{1}13 \rangle$. Although the two latter pyramidal slip system families are not very different from each other, they have distinct effects on the texture due to their different slip activities. In the present simulation work they can carry up to 30% of the total slip, with more slip in type I than in type II. Based on previous studies on pure Mg [38,39], the set of reference stresses [1, 8, 8, 6, 6] was chosen to set their relative strengths, where the values refer to the slip system families in the order $\tau_0^{basal} / \tau_0^{basal}$, $\tau_0^{prism.} / \tau_0^{basal}$, $\tau_0^{pyr.(a)} / \tau_0^{basal}$, $\tau_0^{pyr.(c+a)-I} / \tau_0^{basal}$, $\tau_0^{pyr.(c+a)-II} / \tau_0^{basal}$. For some alloys deviations can appear from the pure Mg reference stresses [38,40]. For example, in Beausir et al. [40] the best simulation results were obtained for the set [1, 8, 8, 4.5, 4.5] for AZ71. The strain rate sensitivity index value $m = 0.1$ was used, which is an approximate average value for pure Mg and Mg alloys according to several measurements [40,41]. This set of reference stresses and of strain rate sensitivity value will be used throughout this study. The m value was considered to be the same as the strain rate sensitivity exponent of slip in the constitutive slip law [42]:

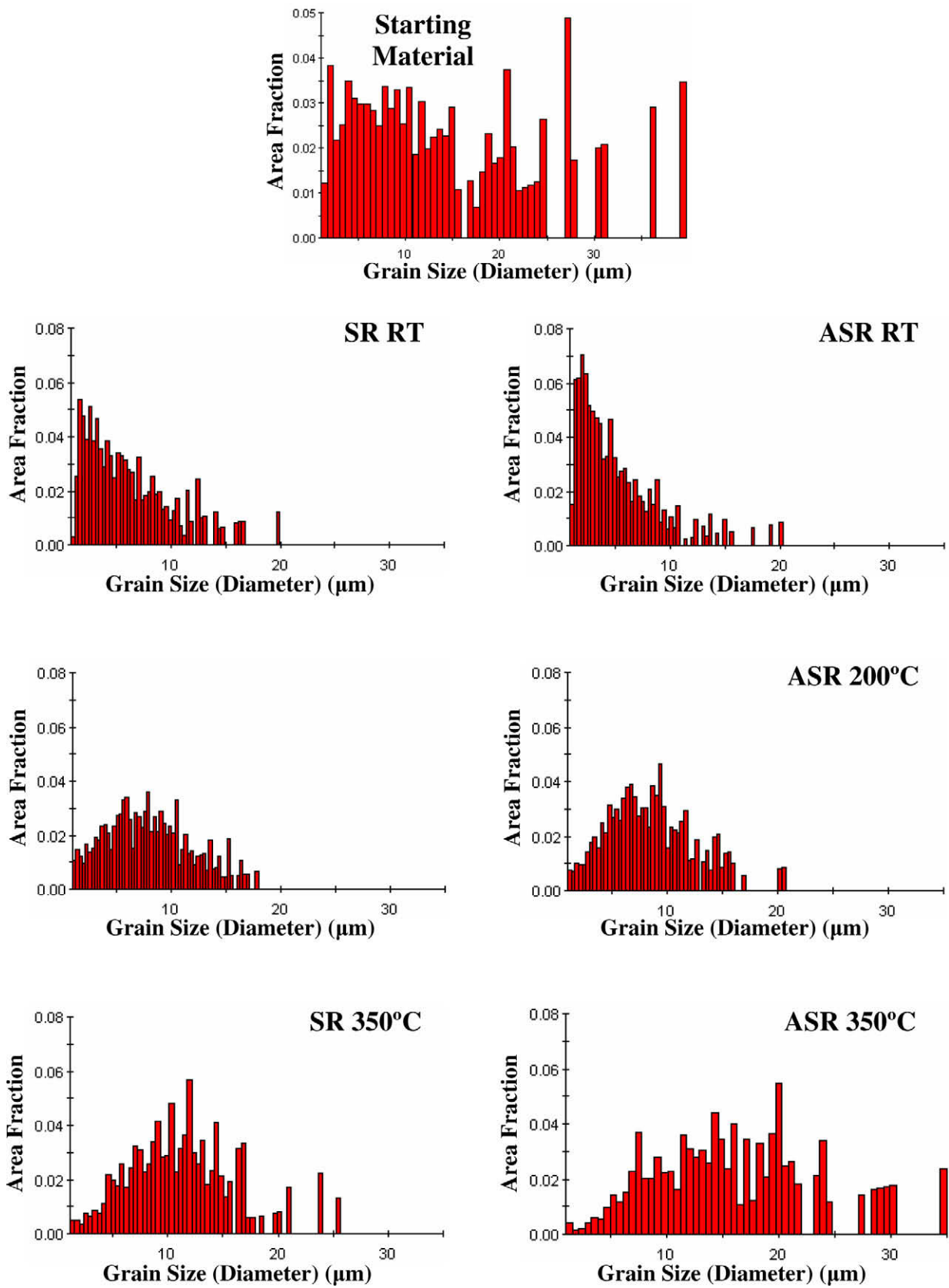


Fig. 4. Grain size distribution after two passes of rolling.

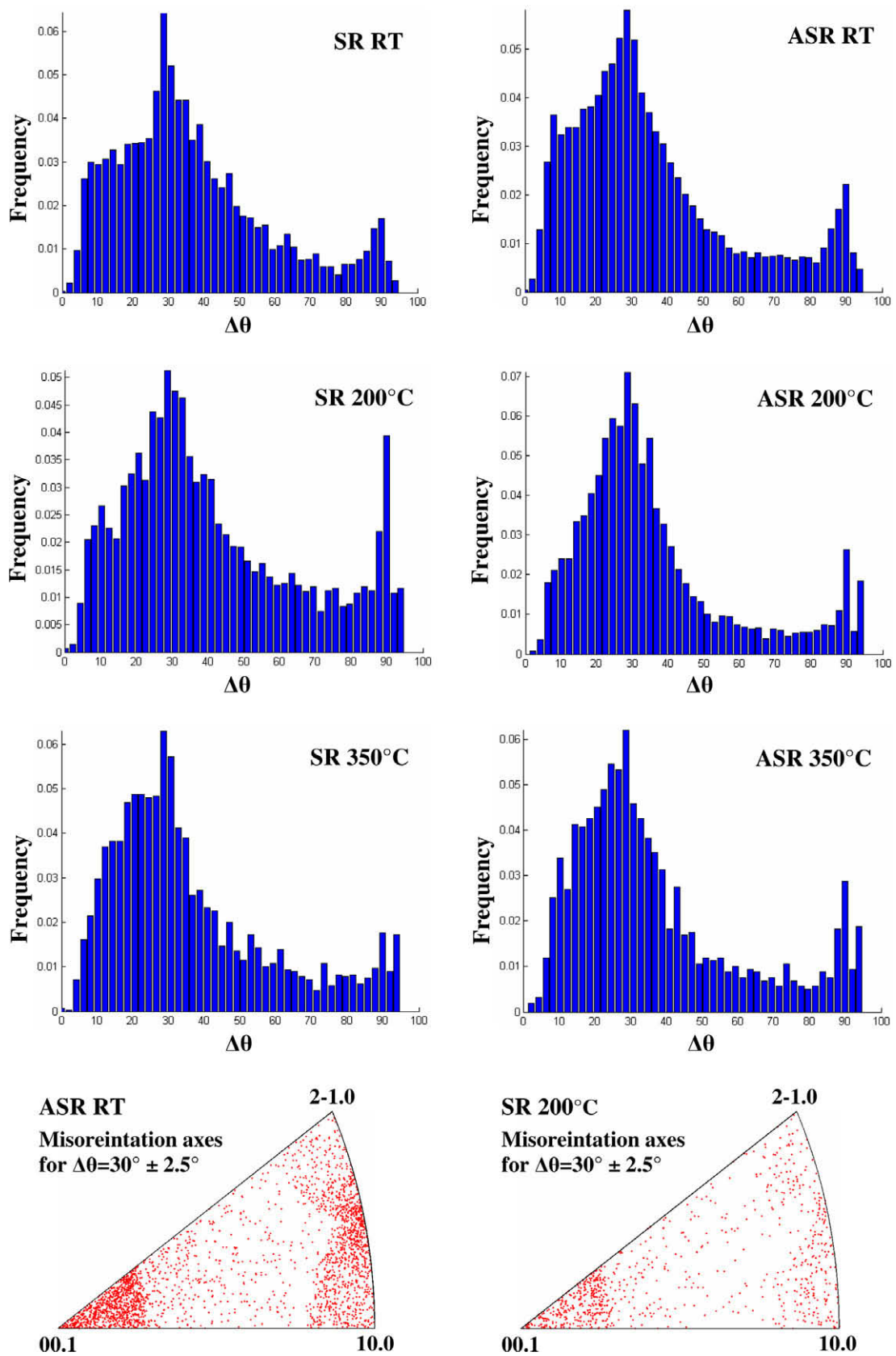


Fig. 5. Misorientation distribution of the first neighbours after two passes of rolling.

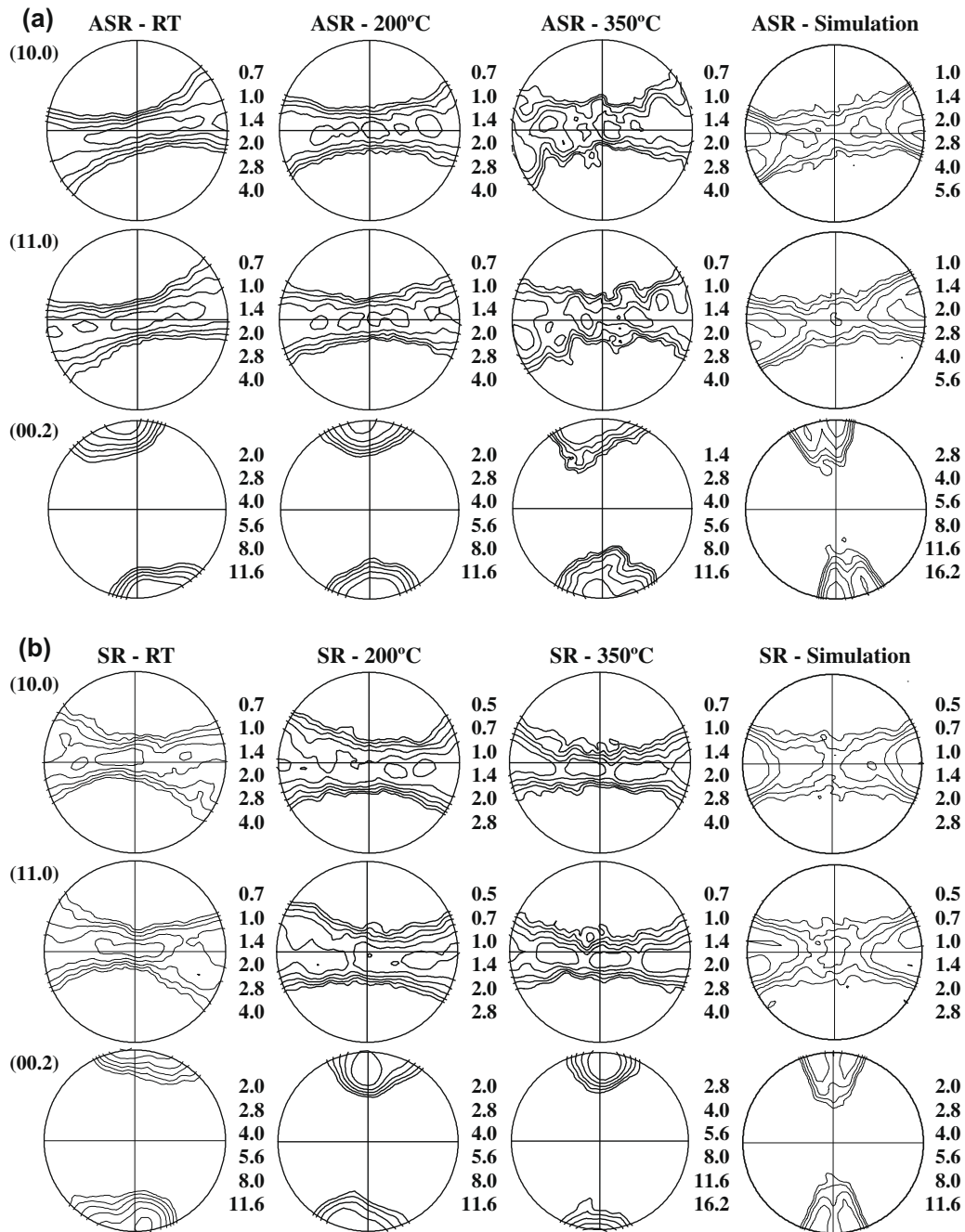


Fig. 6. (10.0), (11.0) and (00.2) pole figures of experimental and simulated textures after the second asymmetric rolling pass (a) and symmetric rolling (b) of pure magnesium. RD, right; ND, top; TD, projection plane.

$$\tau^{s,f} = \tau_0^f \text{sgn}(\dot{\gamma}^{s,f}) \left| \frac{\dot{\gamma}^{s,f}}{\dot{\gamma}_0} \right|^m = \tau_0^f \frac{\dot{\gamma}^{s,f}}{\dot{\gamma}_0} \left| \frac{\dot{\gamma}^{s,f}}{\dot{\gamma}_0} \right|^{m-1} \quad (7)$$

The slip systems are grouped into “families”, for which purpose the index f is used. In Eq. (7) $\tau^{s,f}$ is the resolved shear stress in the slip system indexed s of the family indexed f , $\dot{\gamma}^{s,f}$ is the slip rate and τ_0^f is the reference stress level (at which the slip rate is $\dot{\gamma}_0$). The reference shear rate $\dot{\gamma}_0$ is assumed to be the same for all slip systems. Eq. (7) has been widely used in crystal plasticity simulations [39,43–49]. It is assumed here that the reference shear stress τ_0^f is

the same within a given slip system family, but can be different from one family to another. Slip system hardening due to deformation was not modelled. Deformation twinning was not considered for the two materials in the simulations as very little twinning was observed in the microstructure analysis. Note that there was no allowance made for temperature in the simulations because temperature effects (like dynamic recrystallisation) were not considered in the simulations. Consequently, the same simulation result should be compared with the experimental results at all temperatures.

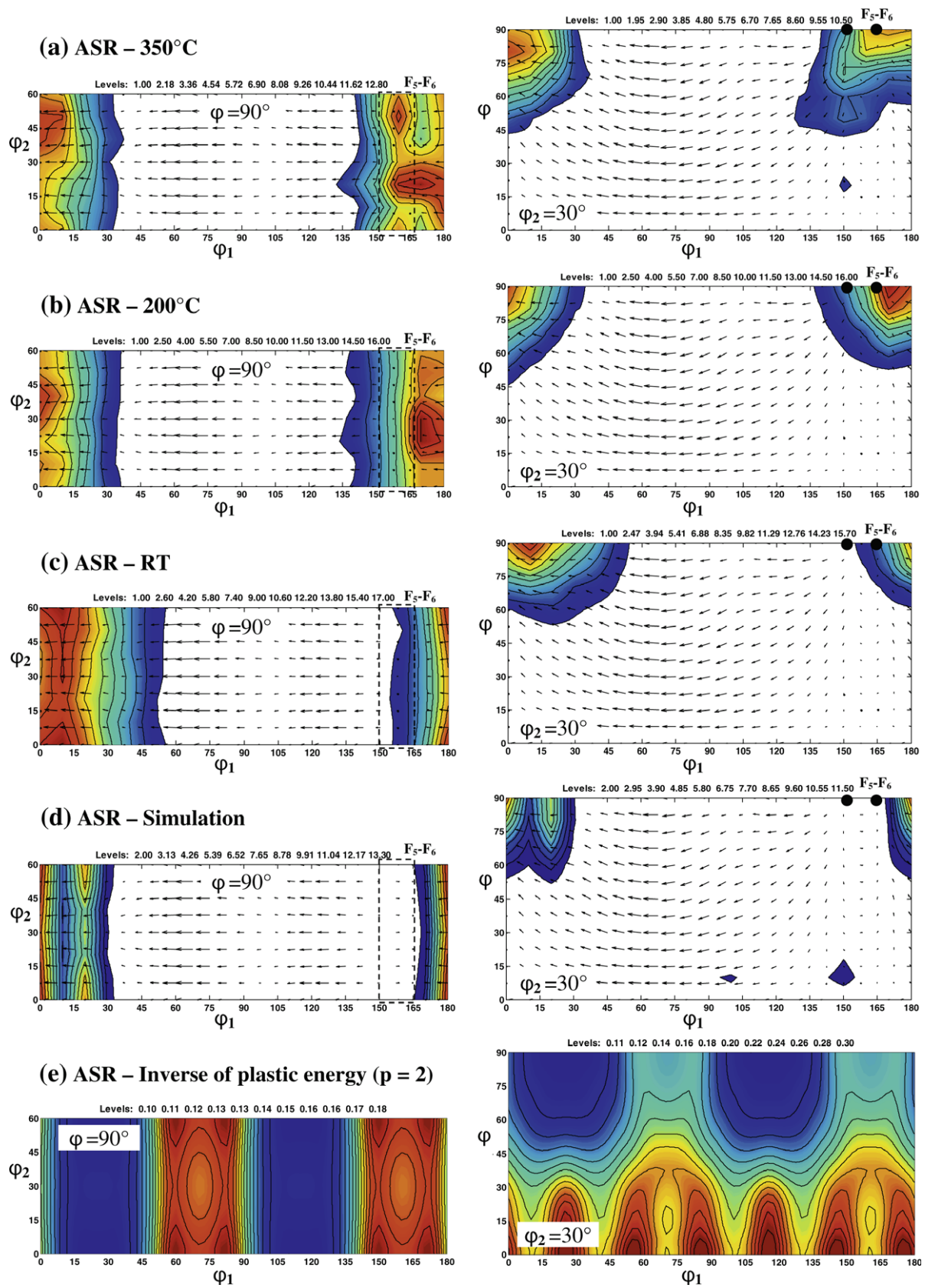


Fig. 7. $\varphi = 90^\circ$ and $\varphi_2 = 30^\circ$ ODF sections of experimental and simulated textures of pure magnesium after asymmetric rolling at 350 °C (a), 200 °C (b) and room temperature (c), with simulated (d) and corresponding energy maps (e).

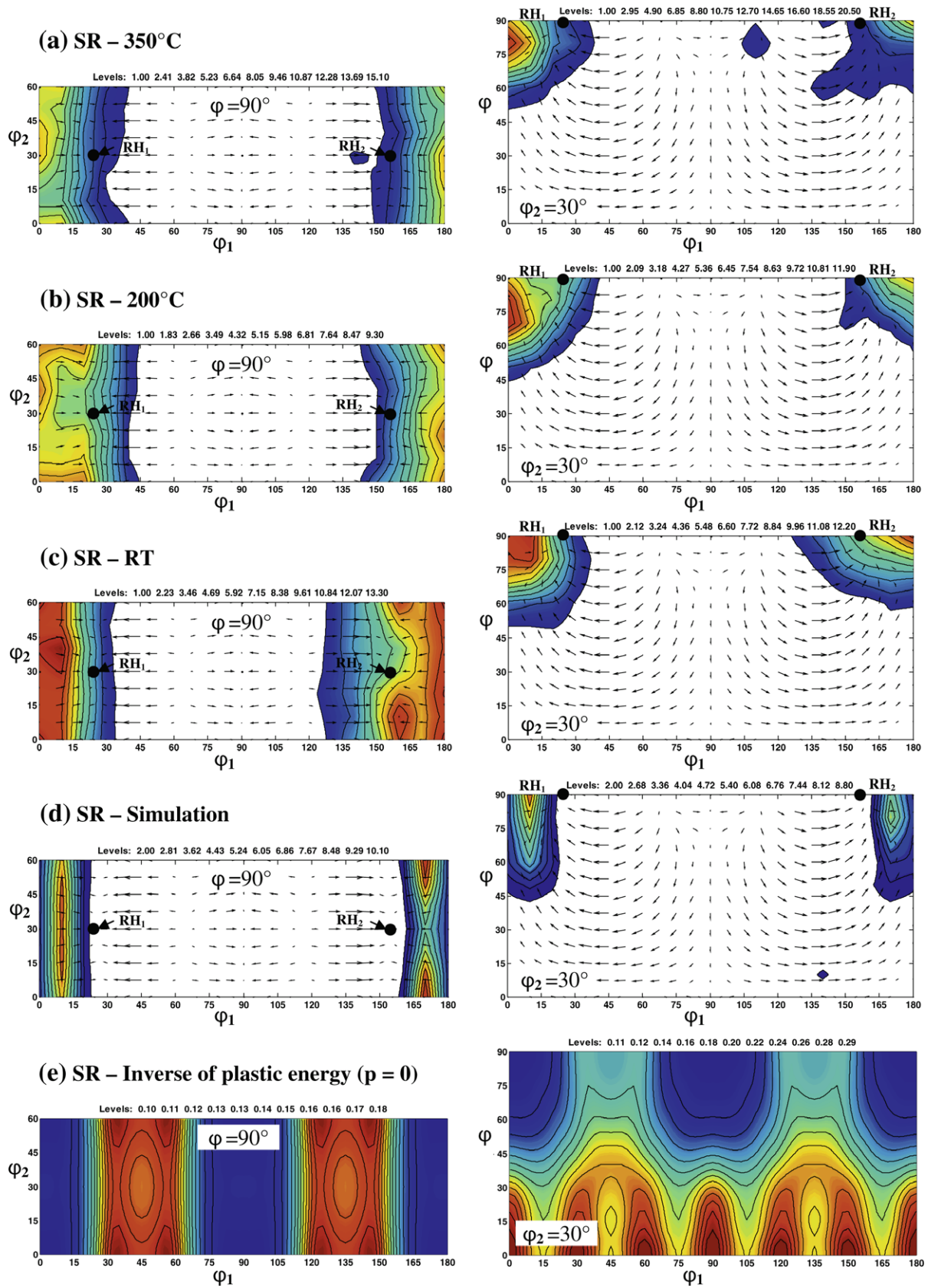


Fig. 8. $\varphi = 90^\circ$ and $\varphi_2 = 30^\circ$ ODF sections of experimental and simulated textures of pure magnesium after symmetric rolling at 350 °C (a), 200 °C (b), room temperature (c), with simulated (d) and corresponding energy maps (e).

Two passes were performed in the simulations and the results obtained after the second pass for ASR and SR are presented as pole figures (Fig. 6a and b, respectively). To obtain a better understanding of the global movement of the grains, the experimental and simulated textures are superimposed on the grain velocity field (see below for more details on the grain velocity field) in the $\varphi = 90^\circ$ and $\varphi_2 = 30^\circ$ ODF sections (Fig. 7 for ASR, Fig. 8 for SR). For both cases, SR and ASR, the main features of texture evolution are quite well reproduced, i.e. rotation of the texture around φ_1 and φ . For SR the simulation results are symmetric with respect to the TD plane due to the symmetry of the process and the initial random texture. In the case of ASR the experimental textures do not display this symmetry, which is also shown in the simulations. However, for the high temperature tests the experimental texture is less well reproduced by the simulations, especially the intensity distribution along the φ_2 direction (see ODF sections $\varphi = 90^\circ$ in Figs. 7a,b,d and 8a,b,d). The φ_2 axis in Euler space represents rotation of the hexagonal crystal unit around its c -axis, i.e. a $\langle c \rangle$ type fibre. The φ_1 and φ angles are constant for such a fibre. As can be seen in Figs. 7 and 8, this fibre is not well reproduced in the 200 °C and 350 °C tests for both ASR and SR. We suggest that this deviation is due to dynamic recrystallization taking place during the 200 °C and 350 °C tests, which will be discussed in Section 6.

5. Stability analysis

The microstructural evidence clearly indicates that dynamic recrystallization (DRX) took place in pure Mg during the present ASR and SR experiments, with a greater impact in the tests at 200 °C and 350 °C. However, the main features of texture evolution can be reproduced without taking into account the process of DRX. In order to understand the effect of DRX in the development of texture, first, texture development will be discussed without taking into account DRX. For this purpose we first carried out an analysis of orientation stability in orientation space.

In order to understand texture evolution it is useful to determine the “stable” orientations of textures. “Stability” here means that the given orientation rotates slowly; it has low lattice spin (Ω). The stability parameter P used in this study is defined as follows (see [49]):

$$P(\underline{g}, \underline{\dot{\epsilon}}) = 1 - (|\Omega(\underline{g}, \underline{\dot{\epsilon}})|/\Omega_{\max})^{1/3} \quad (8)$$

Here $|\Omega(\underline{g}, \underline{\dot{\epsilon}})| = \sqrt{\Omega_{12}^2 + \Omega_{31}^2 + \Omega_{23}^2}$ and Ω_{\max} is the maximum of $|\Omega(\underline{g}, \underline{\dot{\epsilon}})|$ in the whole Euler space. \underline{g} is the orientation defined by (ϕ_1, ϕ, ϕ_2) and $\underline{\dot{\epsilon}}$ is the strain rate. The exponent 1/3 was chosen so that the stability maps look like an ODF. Note that the value of this stability parameter lies between 0 and 1 for “unstable” and “stable” orientations.

However, study of the stability parameter in general is not enough to determine the “ideal” orientations. Ideal here means orientations where the grains will rotate and

will stay. For this purpose, the rotation field and the divergence quantities also have to be examined, especially in the vicinity of “stable” orientations. For completeness of the discussion we first recall the definition of the rotation field and divergence.

The rotation field can be well illustrated by displaying the lattice spin vector defined in orientation space: $\underline{\dot{g}} = (\dot{\phi}_1, \dot{\phi}, \dot{\phi}_2)$. It is obtained from the lattice spin Ω of the real experimental space using the following relations [50,51]:

$$\begin{aligned} \dot{\phi}_1 &= \Omega_{12} - \dot{\phi}_2 \cos \varphi \\ \dot{\phi} &= \Omega_{32} \cos \varphi_1 + \Omega_{13} \sin \varphi_1 \\ \dot{\phi}_2 &= (\Omega_{32} \sin \varphi_1 - \Omega_{13} \cos \varphi_1) / \sin \varphi \end{aligned} \quad (9)$$

The continuity equation describes variations in the orientation density function f , which also gives useful information on the nature of the field. In the Eulerian formulation it is given by:

$$\dot{\gamma} \frac{d \ln f}{d \gamma} + \dot{\phi} \cot \varphi + \text{div}(\underline{\dot{g}}) + \underline{\dot{g}} \cdot \text{grad}(\ln f) = 0 \quad (10)$$

where γ is the strain. The rate of change of the ODF intensity for a given orientation is characterized by $\dot{\gamma} d \ln f / d \gamma$. For relatively weak textures the term $\underline{\dot{g}} \cdot \text{grad}(\ln f)$ can be neglected for the reason that both $\underline{\dot{g}}$ and $\text{grad}(\ln f)$ are small near ideal orientations.

From the viewpoint of texture formation, a texture component for orientation \underline{g} is considered stable during deformation as long as

$$\underline{\dot{g}} = (\dot{\phi}_1, \dot{\phi}, \dot{\phi}_2) = 0 \quad \text{and} \quad \dot{\gamma} \frac{d \ln f}{d \gamma} > 0. \quad (11)$$

The quantity $\dot{\gamma} \cdot d \ln f / d \gamma$ represents the changes which take place in the ODF during plastic strain: in order to shorten the notation this will be termed $\text{div}^{(\phi)}$ because, basically, it is the quantity $\text{div}(\underline{\dot{g}})$ including the correction term $\dot{\phi} \cot \varphi$, which accounts for distortion of the Euler space along the ϕ coordinate. For further details on the rotation field, divergence quantity and continuity equation see Gilormini et al. [51], Arminjon [52] and Clément [53].

The velocity gradient used for SR is defined by Eq. (1), where $\dot{\epsilon} = \sqrt{3}/2$ in order to obtain a von Mises equivalent strain rate of 1.0 s⁻¹. For ASR the velocity gradient defined by Eq. (2) is applied, where $\dot{\epsilon} = \sqrt{3}/(4+p^2)$, and calculations were carried out for different values of the shear coefficient, i.e. $p = 0$ (plane strain), 0.5, 1.0, 2.0 and 50 (practically, the latter represents simple shear).

The stability parameter and the quantity $\text{div}^{(\phi)}$ are calculated in the whole Euler space on a grid of 1° of the three Euler angles while the velocity field is calculated on a grid of 7.5°. Fig. 9 displays the stability parameter defined by Eq. (8), where the velocity field (Eq. (9)) is also superimposed in the $\phi = 90^\circ$ and $\phi_2 = 30^\circ$ sections of Euler space. These two sections allow depiction of the vicinity of all stable orientations for all values of the shear coefficient.

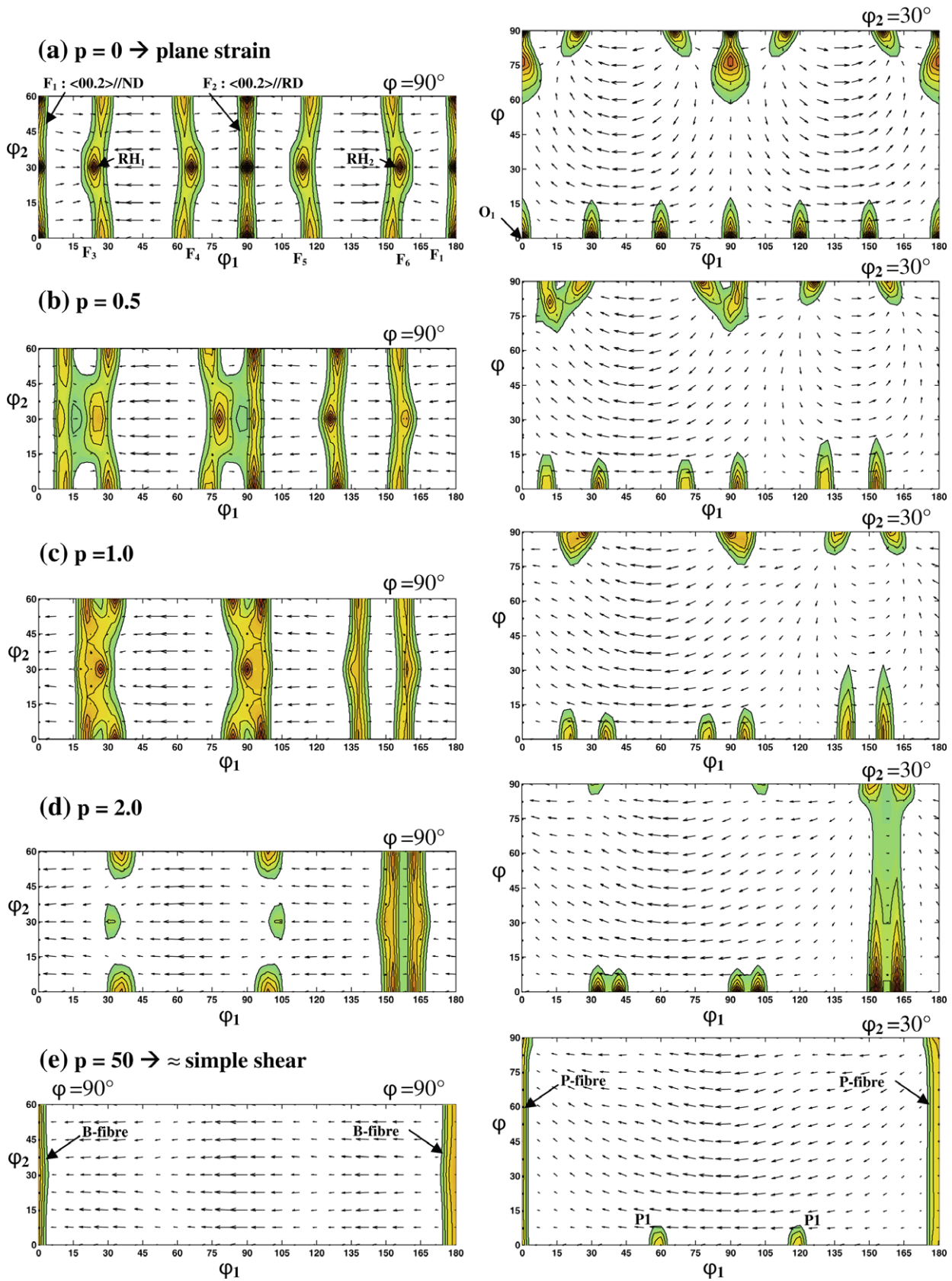


Fig. 9. Orientation stability and velocity field evolution as a function of the asymmetry parameter p in the $\phi = 90^\circ$ and $\phi_2 = 30^\circ$ sections of Euler space. Levels: 0.5 – 0.55 – 0.60 – 0.65 – 0.70 – 0.75 – 0.80 – 0.85 – 0.9 – 0.95 – 1.0.

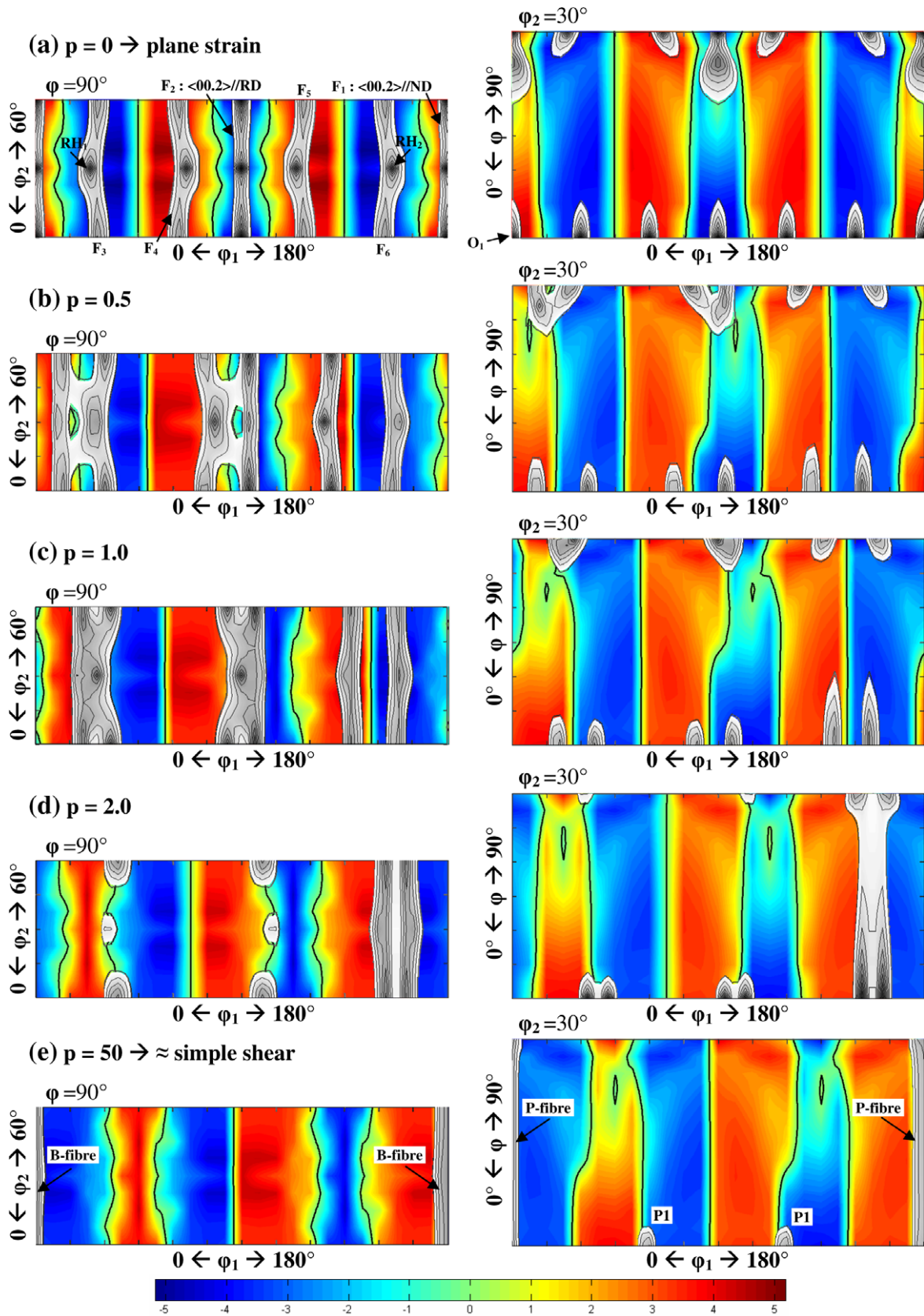


Fig. 10. Divergence maps (negative areas in blue, positive areas in red, bold black line corresponding to $div^{(\phi)} = 0$) superimposed on the stable orientation (black and white) as a function of the asymmetry parameter p in the $\phi = 90^\circ$ and $\phi_2 = 30^\circ$ sections of Euler space. (For interpretation of color mentioned in this figure the reader is referred to the web version of the article.)

Fig. 10 displays $div^{(\phi)}$ maps, with the high stability regions also indicated. The two figures should be examined at the same time to characterize the ideal orientations as a function of the shear coefficient:

1. $p = 0$ (plane strain) (Fig. 9a). From the stability maps one particular orientation, O_1 , and six fibres, F_1 – F_6 , displaying high stability can be identified; they are “ ϕ_2 ” type fibres. A singular orientation appears several times in the $\phi = 0^\circ$ due to the singularity of the Euler space and the hexagonal symmetry. It is defined by $(\phi_1, \phi, \phi_2) = (0^\circ, 0^\circ, 30^\circ)$, which corresponds to the Miller indices $\langle 10.0 \rangle \parallel \text{RD}$ and $\langle 00.2 \rangle \parallel \text{TD}$. The six ϕ_2 fibres are all contained in the $\phi = 90^\circ$ section and appear at $\phi_1 = 0^\circ$ (F_1), 30° (F_3), 60° (F_4), 90° (F_2), 120° (F_5) and 150° (F_6). Along these fibres the stability was not homogeneous, with higher stability appearing at $\phi_2 = 30^\circ$ for all fibres. In the case of fibres F_1 and F_2 higher stabilities also appeared at $\phi_2 = 0^\circ$. If we now look at the velocity field, the lattice rotation velocity is nearly 0 on both the F_1 and F_2 fibres. In the case of the F_1 fibre the grains rotate towards the fibre in the ϕ direction but rotate away from it in the ϕ_1 direction (positively or negatively, depending on the side of the fibre). There is no particular movement in the ϕ_2 direction. In the case of F_2 the reverse is true: the grains rotate towards the vicinity of F_2 in the ϕ_1 direction but rotate away in direction ϕ . Concerning the other fibres, we can distinguish F_3 and F_6 from F_4 and F_5 . From all directions grains will rotate towards F_3 and F_6 with a “preference” for the particular orientation of these fibre at $\phi_2 = 30^\circ$. Once again, the situation is reversed for F_4 and F_5 , with the grains leaving their vicinity in all directions (ϕ_1 , ϕ and ϕ_2). To quantify which orientation is “ideal” we have to look at the quantity $div^{(\phi)}$ in the vicinity of all these fibres (Fig. 10a). F_1 , F_4 and F_5 are located in the area $div^{(\phi)} > 0$, indicating migration of grains out of these regions, thus these high stability fibres cannot be considered ideal orientations. The case of F_2 is more complex. F_2 is located in the area $div^{(\phi)} < 0$, but the sense of the ϕ component of the velocity field indicates a leaving movement in this direction, meaning that, $\partial\dot{\phi}_1/\partial\phi_1 + \partial\dot{\phi}/\partial\phi + \partial\dot{\phi}_2/\partial\phi_2 + \dot{\phi} \cot(\phi) < 0$ but with the term $\partial\dot{\phi}/\partial\phi > 0$, which does not make F_2 an ideal orientation. The situation is similar for the particularly high stability O_1 orientation, where the velocity field in its vicinity is never fully directed towards it and thus it cannot be considered an ideal orientation either. In contrast, F_3 and F_6 present all the characteristics of ideal orientations, i.e. high stability, located in $div^{(\phi)} < 0$ and the sense of the components of the velocity field are all in the direction of the fibres, thus they are ideal orientations for plane strain rolling of hexagonal metals displaying a large proportion of basal glide (the case for Mg). The F_3 and F_6 fibres correspond to $\langle 00.2 \rangle$ at $\pm 30^\circ/\text{ND}$, respectively. It should be noted that two particular preferential orientations of these fibres are located at $\phi_2 = 30^\circ$ and not exactly at $\pm 30^\circ/\text{ND}$ but $\pm 24^\circ/\text{ND}$ with the normal of the prismatic plane parallel to TD. In the following these orientations will be referred to as RH_1 and RH_2 , where “RH” refers to “rolling hexagonal” (see Fig. 9a). Two important aspects of stability and persistence in the case of symmetric rolling is that: (i) all the quantities (stability, velocity field and $div^{(\phi)}$) present perfect mirror symmetry with respect to the $\phi_1 = k \cdot 90^\circ$ planes $k \in \mathbb{N}$; (ii) all the stable orientations are located inside $div^{(\phi)} < 0$ zones. These two aspects together imply that all the grains converge towards stable positions and will not leave those regions under multiple passes of SR, even if the sheet is rotated around ND by $k \cdot 90^\circ$ between passes, because of the mirror symmetry. This feature of the texture reduces the possibility of controlling the deformation texture by SR.
2. $p = 0.5$. F_3 and F_4 rotate towards F_1 and F_2 around $\phi_1 < 0$ and $\phi_1 > 0$, respectively, while F_5 and F_6 move closer. The velocity field and divergence around the stable orientation are only slightly affected. The “ideal” orientation determined in plain strain compression rotates slightly and the persistence characteristics in their vicinity remain the same (i.e. $div^{(\phi)}$ and the velocity field).
3. In the case where the amount of shear is equal to the compression plane deformation, i.e. $p = 1.0$, F_1 and F_3 and F_2 and F_4 are joined. F_5 and F_6 are now separated by about 20° around $\phi_1 = 150^\circ$, but remain within negative and positive divergence areas, respectively. It should be remembered that the fact that the high stable regions are located on the boundary of $div^{(\phi)} < 0$ and $div^{(\phi)} > 0$ areas is a characteristic feature of simple shear texture for hexagonal metals [48], as well as cubic metals [54,55]. For the present value of the shear coefficient ($p = 2$) its impact on the persistence characteristics can be seen for F_1 – F_3 and F_2 – F_4 , which are now located at the boundary of positive and negative divergence regions (Fig. 10c).
4. In the case of $p = 2.0$, which is the case for the present experimental study, F_1 – F_3 and F_2 – F_4 almost disappear and F_5 and F_6 are joined between $\phi_1 = 150^\circ$ and $\phi_1 = 165^\circ$. At the same time, a new fibre appears along the ϕ direction ($0 \leq \phi \leq 90^\circ$ in the $\phi_2 = 30^\circ$ section and at $\phi_1 = 150^\circ$ – 165°). This fibre arises from prismatic activity, as explained in Beausir et al. [48]. The stable orientations and their persistence characteristics for $p = 2.0$ look like those of simple shear but are shifted by about -22.5° along ϕ_1 . The velocity field is mainly oriented around $-\phi_1$ and all the stable orientations are situated on the boundary of divergence/convergence zones.
5. $p = 50$ (Figs. 9e and 10e). The B- and P-fibres (basal and prismatic glide) are obtained in almost the same position as in simple shear [48]. This value of shear coefficient is a “critical” value above which the compression component of the strain can be neglected in terms of texture evolution.

To summarise, in ASR, due to differences in the circumferential velocities of the rollers, an important shear

component with respect to the plane strain is induced in the sheet. This shear component considerably modifies changes in orientation of the grains and the stability characteristics of the texture. The stable positions change and the velocity field becomes more and more directed along the negative ϕ_1 direction. An important fact is that in ASR (i.e. $1 < p < \infty$) the stable orientations are located on the boundary between $div^{(\phi)} > 0$ and $div^{(\phi)} < 0$ zones. Moreover, the velocity field does not display mirror symmetry with respect to the $\phi_1 = k \cdot 90^\circ$ planes ($k \in \mathbb{N}$), i.e. around ND. These two main differences can be exploited to control the deformation texture; indeed, rotation of the sheet by 180° around ND between two passes repositions the grains, accumulated in the initial pass near an ideal orientation, in a positive divergence zone from which the grains will rotate under the second pass. “Routes” (as in ECAE) with an appropriate ratio between the circumferential velocities of the rollers can be chosen in order to “control” the texture of the sheet. Note that the orientation stability studies were repeated for different c/a ratios and relative reference strength sets but the results are not shown here for reasons of brevity. From that it can be said that the stable orientations remains almost the same and that the relative strengths of the slip systems families influence the relative importance of the different ideal orientations.

6. Effect of dynamic recrystallization on texture

The ideal orientations identified in the preceding section are plotted in Figs. 7 and 8. In the case of the room temperature test the grains accumulated in the vicinity of the ideal orientations for both ASR and SR, meaning that dynamic recrystallization does not significantly affect texture evolution. This is why the simulated textures obtained without taking into account the phenomenon of DRX match quite well with the experimental ones.

In the case of the 200 °C and 350 °C ASR and SR tests the processing temperature was higher than the minimum recrystallization temperature ($0.4T_M$). Therefore, it is assumed that full dynamic recrystallization took place in both cases. Equiaxed grains with serrated grain boundaries indicate the occurrence of dynamic recrystallization, although complete dynamic recrystallization might not have occurred (Fig. 5). As mentioned in Section 3.1, in order to investigate the occurrence of dynamic recrystallization the misorientation between each couple of neighbouring grains was calculated. It was found that a large proportion of grains possessed an $\sim 30^\circ$ misorientation with respect to their neighbour in the deformed samples. The misorientation axes for a large proportion of grains was [00.1], which indicates the presence of a large fraction of dynamically recrystallized grains in all the samples. It should be mentioned here that dynamically recrystallized grains in Mg are known to display a 30° misorientation around [00.1] with respect to their neighbours [56–58].

Since the simulations were carried out without considering the effect of DRX, the rotation by 30° around ϕ_2 (“c”-axis) could not be reproduced in the simulated textures. For both the ASR and SR simulations (Figs. 7 and 8) a fibre $(\phi_1, \phi, \phi_2) = (0^\circ, 90^\circ, -60^\circ)$ formed, with the maximum intensity at $\phi_2 = 0^\circ$ and a lower intensity at $\phi_2 = 30^\circ$. In both the experimental ODFs (Figs. 7 and 8) of the 200 °C and 350 °C ASR samples, where dynamic recrystallization took place, the situation was reversed. The maximum intensity of the ODFs was located at $\phi_2 = 30^\circ$ and the minimum at $\phi_2 = 0^\circ$.

In previous studies [40] the DRX process was assumed to be controlled by the plastic energy. For this reason, a map of the inverse of the plastic energy, defined by Eq. (12), is also displayed in Figs. 7e and 8e.

$$E(g) = \left(\sum_f \sum_s \tau^{s,f}(g) \dot{\gamma}^{s,f}(g) \right)^{-1}. \quad (12)$$

Note that the inverse of $E(g)$ is plotted, so the DRX grains are expected to be in those orientations with a high value on these maps (in red¹). First, in these two maps $p = 0$ (SR) and $p = 2$ (ASR), Figs. 8e and 7e, respectively it should be noted that in the $\phi = 90^\circ$ section a local minimum is present all along ϕ_1 at $\phi_2 = 30^\circ$. In the case of ASR (250 °C and 350 °C) (see Fig. 7) the local maximum of the experimental fibre texture corresponds to a local minimum of energy (in red) in both the 200 °C and 350 °C ASR experiments. On the other hand, for the simulated texture the local maximum is located in a local maximum of energy. This further suggests the occurrence of a considerable amount of DRX during the experiments, which is manifests as a rotation of 30° around the c -axis. The main rotation (around TD) imposed by deformation of the grain is well reproduced by the simulation, however, during this rotation some new grains appear and grow due to a discontinuous dynamic recrystallization process. These new grains are oriented following the minimum energy orientations, which leads to a rotation of part of the texture around the c -axis, i.e. around the ϕ_2 Euler angle. These dynamically recrystallized grains are also deformed under the applied loading, therefore they remain along the $(\phi_1, \phi, \phi_2) = (0^\circ, 90^\circ, -60^\circ)$ fibre. The simulations were able to reproduce the position of this fibre but not the $\langle c \rangle$ fibre (rotation around the ϕ_2 axis of the grains) due to dynamic recrystallization. In the case of SR (250 °C and 350 °C) (see Fig. 8) the same behaviour can be observed except that the difference between the local minimum and maximum of the plastic energy is smaller than in ASR. As a consequence, the fibre is more homogeneous.

¹ For interpretation of color in Figs. 2–5 and 7–10, the reader is referred to the web version of this article.

7. Conclusions

The microstructure and texture evolution during asymmetric and symmetric (conventional) rolling of polycrystalline Mg were studied for three rolling temperatures, room temperature, 200 °C and 350 °C, experimentally as well as using simulations. For the interpretation of texture development the ideal orientations, rotation field and divergence quantities were determined for both ASR and SR. Analysis of the results led to the following main conclusions.

An average grain size of $\sim 2 \mu\text{m}$ was observed in the case of room temperature ASR as well as SR. The grain size increased with higher rolling temperature for both cases.

A predominant basal texture $[00.2]||\text{ND}$ developed with the fibre axis parallel to the RD in the case of SR (conventional) samples. However, in all the ASR samples the basal texture was rotated by $\sim 5\text{--}10^\circ$ anticlockwise from ND.

Differences in the mechanisms of texture evolution during ASR and SR are presented. Continuous accumulation of grains with ideal end orientations is expected during multi-pass SR. The persistence characteristics of ideal orientations in ASR (i.e. $1 < p < \infty$) are: (i) their location on boundaries of positive/negative divergence zones and (ii) their velocity field does not display mirror symmetry with respect to the $\phi_1 = k \cdot 90^\circ$ plane $k \in \mathbb{N}$, i.e. around ND, which offers the possibility of applying different “routes” to control the final texture.

Dynamic recrystallization took place during both ASR and SR, which was shown through microstructural characterization, with the help of misorientation distribution plots, and by comparing the experimental and simulated textures (DRX was not considered in the simulations). The classical rotation by 30° around the c -axis ($\phi_2 = 30^\circ$) due to recrystallization was clearly confirmed at 200 °C and 350 °C.

Acknowledgements

The authors Benoît Beausir, Somjeet Biswas and Satyam Suwas would like to acknowledge the Department of Science and Technology (DST), Government of India, for providing the financial grant that was used to carry out this research. The work also used the facilities of the Institute Nano-Science Initiative (INI) sponsored by the DST-FIST programme at IISc, Bangalore. The authors thank Prof. Hu-Chul Lee of Seoul National University for the use of an asymmetric rolling mill.

References

- [1] Stalman A, Sebastian W, Friedrich H, Schumann S, Dröder K. *Adv Eng Mater* 2001;3:969.
- [2] Kainer KU, Von Buch F. In: Kainer, KU, editor, *Magnesium alloys and technologies*. Weinheim: Wiley-VCH; 2003.
- [3] Berbon PB, Tsenev NK, Valiev RZ, Furukawa M, Horita Z, Nemoto M, et al. *Metal Mater Trans* 1998;29:2237.
- [4] Eddahbi M, Ruano OA. *Rev Metal* 2006;42:146.
- [5] Mathis K, Gubicza J, Nam NH. *J Alloys Compd* 2005;392:194.
- [6] Chang SY, Lee SW, Kang KM, Kamado S, Kojima Y. *Mater Trans* 2004;45:488–92.
- [7] Furukawa M, Oh-ishi K, Komura S, Yamashita A, Horita Z, Nemoto M, et al. *Towards Innovation in Superplasticity II* 1999;304:97.
- [8] Nemoto M, Horita Z, Furukawa M, Langdon TG. *Towards Innovation in Superplasticity II* 1999;304:59.
- [9] Harai Y, Kai M, Kaneko K, Horita Z, Langdon TG. *Mater Trans* 2008;46:76.
- [10] Kai M, Horita Z, Langdon TG. *Mater Sci Eng* 2008;488:117.
- [11] Horita Z, Langdon TG. *Scripta Mater* 2008;58:1029.
- [12] Wang QF, Xiao XP, Hu J, Xu WW, Zhao XQ, Zhao SJ. *J Iron Steel Res, Int* 2007;14:167.
- [13] del Valle JA, Pérez-Prado MT, Ruano OA. *Mater Sci Eng A* 2005;410:353.
- [14] Pérez-Prado MT, del Valle JA, Ruano OA. *Scripta Mater* 2004;51:1093.
- [15] Suwas S, Gottstein G, Kumar R. *Mater Sci Eng A* 2007;471:1.
- [16] Watanabe H, Mukai T, Ishikawa K. *J Mater Proc Technol* 2007;182:644.
- [17] Kim SH, You BS, Yim CD, Seo YM. *Mater Lett* 2005;59:3876.
- [18] Huang X, Suzuki K, Watazu A, Shigematsu I, Saito N. *J Alloys Compd* 2009;470:263.
- [19] Huang X, Suzuki K, Watazu A, Shigematsu I, Saito N. *J Alloys Compd* 2009;479:726.
- [20] Huang X, Suzuki K, Saito N. *Mater Sci Eng* 2009;508:226.
- [21] Huang X, Suzuki K, Watazu A, Shigematsu I, Saito N. *J Alloys Compd* 2008;457:408.
- [22] Huang X, Suzuki K, Watazu A, Shigematsu I, Saito N. *Mater Sci Eng* 2008;488:214.
- [23] Lee SH, Lee DN. *Int J Mech Sci* 2001;43:1997.
- [24] Kim KH, Lee DN. *Acta Mater* 2001;49:2583.
- [25] Kim SH, Lee JK, Lee DN. In: *Proc. ultrafine grained materials 2002, TMS annual meeting*. Warrendale (PA): TMS; 2002.
- [26] Kim SH, Ryu JH, Kim KH, Lee DN. *Mater Sci Res Int* 2002;8:20.
- [27] Lapovok R, Tóth LS, Winkler M, Semiatin SL. *J Mater Res* 2009;24:459.
- [28] Underwood EE. *Quantitative stereology*. Reading, (MA): Addison-Wesley; 1970.
- [29] Dođruoğlu AN. *J Mater Process Technol* 2001;110:287.
- [30] Sezek S, Aksakal B, Can Y. *Mater Des* 2008;29:643.
- [31] Beausir B, Tóth LS, Bouaziz O. *Mater Sci Forum* 2005;495:1603.
- [32] Beausir B, Tóth LS. In: *Proceeding of International Conference on Microstructure and Texture in Steel (MATS08)*, Tata Steel Jamshepur, India, 5–7 February 2008, Springer, in press.
- [33] Sidor J, Miroux A, Petrov R, Kestens L. *Acta Mater* 2008;56:2495.
- [34] Jin H, Lloyd DJ. *Mater Sci Eng A* 2007;465:267.
- [35] Lee SH, Lee DN. *Int J Mech Sci* 2001;43:1997.
- [36] Lee JK, Lee DN. *Int J Mech Sci* 2008;50:869.
- [37] Zhang F, Vincent G, Sha YH, Zuo L, Fundenberger JJ, Esling C. *Scripta Mater* 2004;50:1011.
- [38] Agnew SR, Mehrotra P, Lillo TM, Stoica GM, Liaw PK. *Acta Mater* 2005;53:3135.
- [39] Beausir B, Suwas S, Tóth LS, Neale KW, Fundenberger JJ. *Acta Mater* 2007;56:200.
- [40] Beausir B, Tóth LS, Qods F, Neale KW. *J Eng Mater Technol* 2009;131:011108-1.
- [41] Agnew SR, Duygulu O. *Int J Plast* 2005;21:1161.
- [42] Kim WJ, Chung SW, Chung CS, Kum D. *Acta Mater* 2001;49:3337.
- [43] Asaro RJ, Needleman A. *Acta Metall* 1985;33:923.
- [44] Neale KW, Tóth LS, Jonas JJ. *Int J Plast* 1990;6:45.
- [45] Van der Giessen E, Wu PD, Neale KW. *Int J Plast* 1992;8:773.
- [46] Tóth LS, Gilormini P, Jonas JJ. *Acta Metall* 1988;36:3077.
- [47] Tóth LS, Jonas JJ, Neale KW. *Proc Roy Soc Lond* 1990;427:201.
- [48] Beausir B, Tóth LS, Neale KW. *Acta Mater* 2007;55:2695.
- [49] Arzaghi M, Beausir B, Tóth LS. *Acta Mater* 2009;57:2440.
- [50] Clément A, Coulomb P. *Scripta Metall* 1979;13:899.
- [51] Gilormini P, Tóth LS, Jonas JJ. *Proc Roy Soc Lond* 1990;430:489.

- [52] Arminjon M. *Acta Metall* 1987;35:615.
- [53] Clément A. *Mater Sci Eng* 1982;55:203.
- [54] Tóth LS, Neale KW, Jonas JJ. *Acta Metall* 1989;37:2197.
- [55] Baczynski J, Jonas JJ. *Acta Mater* 1996;44:4273.
- [56] Ion SE, Humphreys FJ, White S. *Acta Metall* 1982;30:1909.
- [57] Galiyev A, Kaibyshev R, Gottstein G. *Acta Mater* 2001;49:1199.
- [58] Tan JC, Tan MY. *Mater Sci Eng A* 2003;339:124.